

DOI: 10.1002/adfm.200700162

# Direct Observation of Super-Plasticity of Beta-SiC Nanowires at Low Temperature\*\*

By Yuefei Zhang, Xiaodong Han,\* Kun Zheng, Ze Zhang,\* Xiaona Zhang, Jingyong Fu, Yuan Ji, Yajuan Hao, Xiangyun Guo, and Zhonglin Wang

Super-plasticity of single-crystal beta-SiC [111] nanowires for >200 % elongation was observed by in situ axial-tensile experiments in a scanning electron microscope. The SiC nanowires were characterized by a bamboo-like structure appearing as the 3C structured segments intergrowth along the nanowire. The axial localized plasticity and super-plasticity are suggested to result only from the 3C segments, through dislocation generation, propagation and amorphization in contrast to the highly defected structural segments that conduct elastic-deformation only, owing to the lack of slip systems. These results provide key information for understanding the mechanical behavior of SiC nanowires.

## 1. Introduction

Super-plasticity is the ability of a material to exhibit an exceptionally large strain deformation rate during extensile deformation process.<sup>[1]</sup> Ceramics and semiconductors, at room temperature, or more specifically below a transition temperature, behave as nearly ideal brittle solids that fail due to fracture without evidence of plastic deformation.<sup>[2,3]</sup> SiC, as a reinforcing material behave with high hardness, high strength and high stiffness but brittleness. Bulk SiC ceramic material can transform to be ductile above 1000 °C.<sup>[4,5]</sup> Nanomaterials at the one dimensional (1D) form have showed some unusual properties such as the extreme high strength,<sup>[6]</sup> good flexibility,<sup>[7]</sup> fracture toughness<sup>[8]</sup> and inverse Hall-petch effect.<sup>[9]</sup> As a wide bandgap semiconductor material, SiC nanowires (SiCNWs) are very attractive for applications in nanoelectronics that are able to be operated at high temperatures, high powers, high fre-

quencies, and in harsh environments.<sup>[10–12]</sup> For the practical use of SiC NWs, it is fundamentally important not only to investigate electronic properties, but also to understand mechanical properties, such as elastic-plastic response, brittle-ductile transition (BDT).<sup>[13]</sup> The mechanical properties of semiconductor nanowires can be rather different from those of bulk materials. Making a complete elucidation of these properties would be especially important.<sup>[14,15]</sup> Atomistic molecular dynamics (MD) simulations can provide detailed information about dislocation motion, crack branching, fracture, and BDT of nanowires.<sup>[16–18]</sup> However, ambiguous results have emerged; for example, brittle-fracture features with small strain were predicted by molecular dynamics (MD) simulations<sup>[19,20]</sup> for SiC. In contrast, large strain elasticity and ductile fracture features have been observed.<sup>[21,22]</sup> Obviously, experimental studies are required to clarify the true deformation features and mechanisms of the semiconductor nanowires. Researchers have investigated the mechanical properties of various nanowire systems using different techniques, such as nanoindentation,<sup>[23,24]</sup> atomic force microscopy (AFM)<sup>[6,8]</sup> and transmission electron microscopy (TEM).<sup>[7,25]</sup> In situ experiments provide direct visualization and description of the events as they happen and give qualitative information about the structure of deformation. Our previous studies using ex situ<sup>[26]</sup> and in situ<sup>[27]</sup> bending technique have shown low-temperature large strain plasticity of single-crystal SiC NW. However, the plastic strain was not quantified and the fracture process on SiC NWs was not studied due to difficulties in bending testing in transmission electron microscopy (TEM).<sup>[27]</sup> In the present investigation, the nanoscale plastic deformation and fracture experiments on individual SiC NW have been observed by our recent developed in situ stretching equipment in a scanning electron microscope (SEM). A super-plasticity of >200 % has been observed for the first time for SiC nano-wires at low temperature ( $\leq 80$  °C). Our results are critical for understanding the intrinsic and/or universal mechanical properties of the materials with tetrahedral-covalence-bonded structure at small size.

[\*] Prof. X. D. Han, Prof. Z. Zhang, Y. F. Zhang, K. Zheng, Dr. X. N. Zhang, J. Y. Fu, Prof. Y. Ji  
Institute of Microstructure and Property of Advanced Materials  
Beijing University of Technology  
100022 Beijing (P.R. China)  
E-mail: xdhan@bjut.edu.cn; zezhang@bjut.edu.cn

Dr. Y. J. Hao, X. Y. Guo  
Key Laboratory of Coal Conversion, Institute of Coal Chemistry  
Chinese Academy of Sciences  
Taiyuan 030001 (P.R. China)

Prof. Z. L. Wang  
School of Materials Science and Engineering  
Georgia Institute of Technology  
Atlanta, GA 30332 (USA)

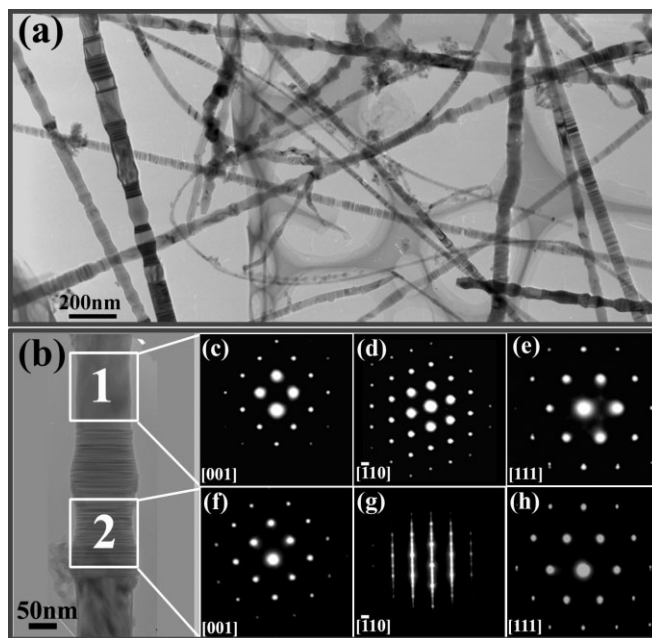
[\*\*] The research was supported by National 973 program under the number of 2002CB613500, Beijing Education Committee Program of 05102001200501 and Funding Project for Academic Human Resources Development in Institutions of Higher Learning under the Jurisdiction of Beijing Municipality. This research was also supported by program for New Century Excellent Talents in University. The authors thanks the help of Mrs. Yinqi Zhang of operating the SEM

## 2. Results and Discussion

### 2.1. The Structure and Substructures of the As-Synthesized Silicon Carbide Nanowires

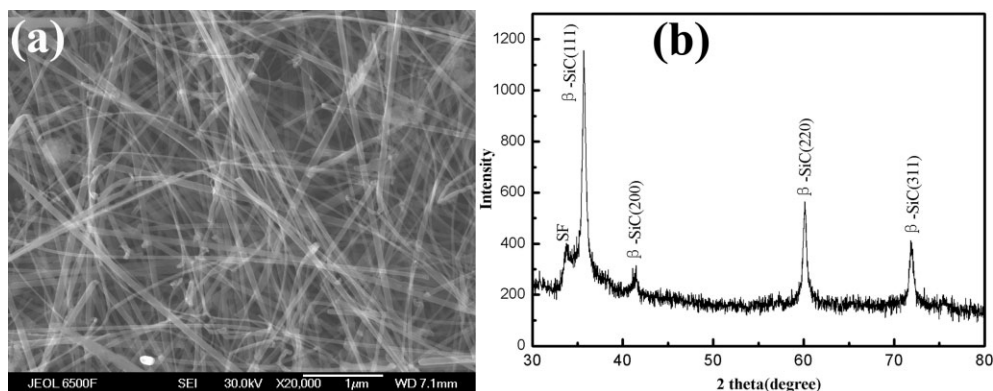
Figure 1a shows the general morphology of the SiC nanowires under SEM observation. The X-ray diffraction pattern indicates the well-developed cubic (3C) structure (with stacking faults) of the SiC NWs as shown in Figure 1b. The average SiC NWs have a length of several tenths of microns and with a diameter up to 150 nm. To have a close view and detail study of the structure and substructures of the SiC NWs, the SiC NW specimens were studied by traditional TEM. Figure 2a is a general morphology of the SiC NWs under TEM observation and Figure 2b is a magnified image of a SiC NW showing that the NW consists of two type intergrowth segments as indicated by 1 and 2. Figure 2c–e shows the corresponding electron diffraction patterns (EDPs) taken from area 1 along zone axes of [001],  $[-110]$ , and [111], respectively, and Figure 2f–h are the [001],  $[-110]$ , and [111] zone axis diffraction patterns taken from area 2. We may notice that, in the reciprocal space, the diffraction patterns along [001] and [111] zone axis show no obvious difference for segment 1 and 2 while there are long streaks along the  $[111]^*$  reciprocal direction in the  $(-110)^*$  reciprocal plane in Figure 2g. As revealed latter in the high-resolution EM (HREM) image of Figure 3, the segment 1 possesses typical 3C structure with an atomic stacking sequence of ABCABC... and segment 2 has disordered structure along [111] direction, i.e., it has stacking-faulted sequence of (111) plane which is along the longitude growth axis of the NW. Here we denote the structure in region 2 of Figure 2b as one dimensional disordered (ODD) or high defective (HD) structure. To confirm the structure difference of the two intergrowth segments of the SiC NWs, we conduct HREM analysis and electron energy loss spectroscopy (EELS) as well as energy dispersive X-ray (EDS) studies.

Figure 3a is a HREM image taken along the  $[-110]$  zone axis from a SiC NW containing both of 3C structural and ODD/HD segments. Obvious distinctive atomic structure can be revealed in the HREM images for regions 1 and 2 which correspond to 3C structure and HD structure, respectively. The fast Fourier



**Figure 2.** a) Typical morphologies of the SiC NWs under TEM observation; b) is a selected piece of SiC NW showing the intergrowth feature with 3C and ODD/HD substructure segments. c)–e) Are the [001],  $[-110]$ , and [111] zone axis EDPs taken from area 1 of (b) and f)–h) are the EDPs taken from area 2 of (b).

transformed (FFT) diffraction patterns of regions 1 and 2 are shown as insets of Figure 3a in the bottom left and bottom right corner, respectively. Figure 3b and c are the enlarged HREM images taken from the red and blue framed areas of Figure 3a. The two dimensional projected atomic structural models are inserted in Figure 3b and c for the 3C and ODD/HD structures, respectively. Based on these structural models, the simulated HREM images are overlaid as insets in Figure 3b and c for the regions of 1 and 2. The simulated HREM images agree well with the experimental recorded HREM images. The white dots in the HREM images represent the holes among atoms and the dark-gray regions are those of Si-C atomic pair projections.<sup>[28]</sup> It is revealed that the 3C-SiC structure repeats



**Figure 1.** a) Typical morphologies of the SiC NWs from SEM observation. b) XRD diffraction pattern indicating the SiC structure is cubic with stacking faults.

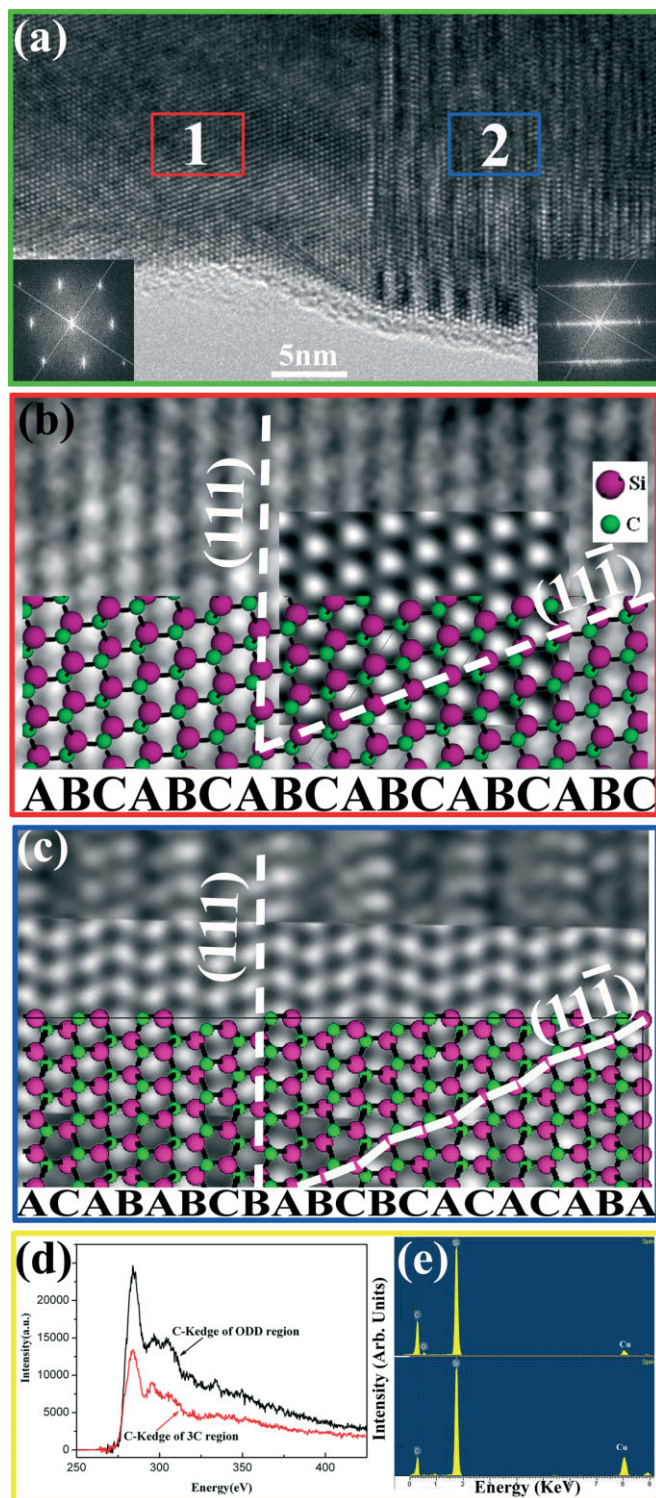


**Figure 3.** a) is the HREM image of a SiC NW showing the intergrowth segments of 3C and ODD/HD structures at the atomic level. The FFT diffraction patterns for the area 1 and 2 are shown as insets in the left bottom corner and right bottom corner, respectively. b) and c) Are the enlarged HREM images showing more clearly the atomic structure of 3C and ODD/HD structures. The atomic structural models and the simulated HREM images based on these models are overlaid in the corresponding figures. d) Are the EELS spectra for Carbon K edge for the 3C and ODD/HD structure segments and e) shows the EDS spectra taken from the regions 1 and 2 of (a). See text for details.

the stacking sequence by ABCABCABC... while the HD structure disturbs the correct stacking sequence ABC but with the random order of ABC such as ACABABC... It is worthwhile to notice that the ABCABC stacking sequence of 3C structure creates straight atomic plane structures along all of the (111), (11-1), (1-11) and (-111) planes, i.e., there are translational symmetry and periodicity in these planes. In contrast, for the stacking sequence of ACABABC..., the translational symmetry and periodicity were broken in the three sets of (1-11), (11-1), and (-111) planes. Here A, B, C represents the three basic structure modules of tetrahedral bonding in SiC.<sup>[29]</sup> As revealed latter in this study, these two segments behave sharp different mechanical properties when external force is loaded from the axial direction.

To finally confirm the regions 1 and 2 are only showing structural difference other than compositional variation, we conducted both of EELS analysis and EDS studies on the regions of 1 and 2 of Figure 3a. Figure 3d shows the EELS spectrums taken from the areas 1 and 2, respectively, and Figure 3e shows the EDS results taken from the above two regions. The EDS results indicate that both regions contain Si and C elements and the ratio of Si and C element keeps the same quantitatively. The Cu element comes from the supporting Cu TEM grid. The EELS spectrums do so slight variance which could come from the distinctive electronic structures of these two type structures.

## 2.2. In-Situ Tensile Testing in the SEM

Following the structure and substructure determination of the SiC NWs, we conducted the in situ tensile tests inside a FEI Quanta 200 ESEM with our home-built nano tensile-testing stage. Two thermal bimetallic strips were mounted on the opposing position of the heating stage. The bimetallic strip is made of two materials with different thermal expansion coefficients. To achieve a significant deflection at lower operational temperature, the two materials must have a large mismatch in thermal expansion coefficients. The bimetallic strips were induced to bend by heating from a filament. The bimetallic strip was made of  $Mn_{72}Ni_{10}Cu_{18}$  and  $Ni_{36}$  with the thermal expansion coefficients of  $26 \times 10^{-6} K^{-1}$  and  $2.9 \times 10^{-6} K^{-1}$ , respectively. The movable part of the bimetallic strips which had a rectangle shape was 20 mm long, 3 mm wide and 0.25 mm in thickness. The bimetallic strip was operated below  $150^\circ C$  to avoid damage to sample. A significant deflection was clearly visible under the gentle heating conditions. The detailed experimental setup is schematically shown in Figure 4.

The as-synthesized NWs were scattered between the two manipulators. Randomly distributed nanowires can be occasionally bridged across the two manipulators. We selected and analyzed nanowires that bridged on the manipulators at an approximate right angle. The SiC NWs are long and straight and they tangled and bridged across the two manipulators. We employed two means to "hold" the NWs on the manipulators tightly. One is the friction force among the NWs (this force is very big due to the tangling features of the long SiC NWs). The other is "soldering" using the electron beam to create "contam-

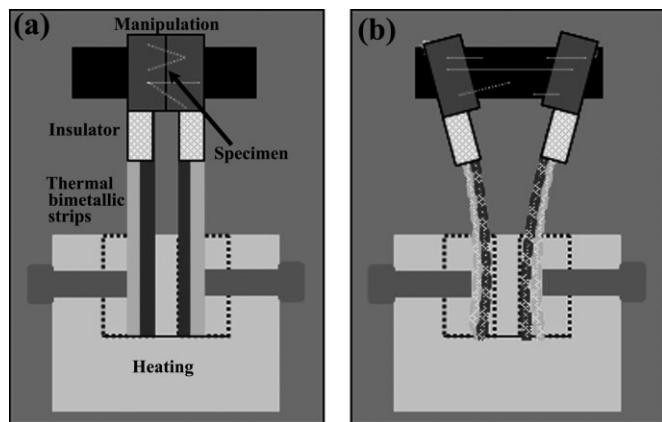


**Figure 4.** a) Schematic illustration of the tensile tool prior to extensile experiment with the SiC NWs scattered on the manipulator. b) The conducting extensile experiment on the SiC NWs (top view).

ination” points on the contact locations of NWs/manipulators. Combining these two methods, the manipulators can hold the NWs tightly without NW’s slipping during extensile experiments. With heating the bimetallic strips, the manipulators were then gradually moved away. A continuously increased temperature (up to 80 °C) drove the manipulator so that a tensile load was applied to extend the clamped nanowire until fracture occurred. Currently we do not have any means to record the tensile load or strain during the testing. We relied on images analysis of a series of SEM images taken during the tensile processes for calculating the maximum fracture strain and image fracture surface. One point worthwhile to mention is that the manipulators were continuously to be driven to move away and the “soldered” SiC NWs were gradually to be flattened (zero strain), then elastically extended with large strain and lately plastically deformed, finally fractured. We carefully checked the series images and started the calculation after the image with SiC NWs being completely flattened.

In this study, eight single SiC NWs were pulled by the bimetallic extensor and the entire process was recorded in situ by SEM imaging. All of the NWs showed extremely large tensile strain (with an average fracture strain  $\geq 25\%$ ) and plastic deformation characters. Figure 5a–g demonstrates a representative experiment in which a SiC NW was suspended and clamped between the two bimetallic actuating manipulators. The manipulators were used to gently pull the SiC NW to increase the strain with increasing temperature from 30 °C to 80 °C. The strain rate was estimated to be about  $5 \times 10^{-4}$  which is the same order as in our previous study.<sup>[27]</sup> A 25  $\mu\text{m}$  long, 96 nm diameter SiC NW was axially extended and broken in the middle. The resulting fragment attached on the left had a length of at least 22  $\mu\text{m}$ , whereas the fragment on the right side had a length of at least 10  $\mu\text{m}$ . Thus, the sum of the fragment lengths far exceeded the original section length. As revealed in Figure 5g

of the fracture tip of the broken SiC NW, there is an abrupt diameter change along the tensile direction which indicates a plastic deformation features.

From the series images of Figure 5, the total length of the SiC NW prior to the extensile experiment was measured to be  $L = 25 \mu\text{m}$ , an elongation of  $T = 7 \mu\text{m}$  was received after tensile testing. This derives an average elongation rate of  $T/L = 28\%$ . However, locally, as indicated by a set of paired arrowheads, the local elongation rate of the SiC NW exceeds 200%. As indicated by a pair of white arrowheads by tracking the reference nodes on the nanowire in the images shown in Figure 5, we measured the starting segment length by  $L_0$  as indicated in Figure 5b. The near end final length of the tracked super-extended segment is indicated by  $l_f$  in Figure 5e. The local elongation rate of the SiC NW is calculated by  $(l_f - L_0)/L_0$ . With  $L_0 = 1.5 \mu\text{m}$  and  $l_f = 4.8 \mu\text{m}$ , the local elongation rate of the SiC NW is close to 220%, showing a super-plastic deformation strain. Figure 5g is a magnified back scattering electron (BSD) image of the broken tip showing a clear slender feature (the top end has been curvily bent). The diameter was reduced 2-fold in average from 96 nm to 50 nm. Assuming the volume fraction remaining constant prior to and after the plastic deformation, the 2-fold diameter reduction agrees well with the  $\sim 200\%$  elongation in length. The diameter of the plastically deformed region is identical, indicating a uniform deformation process. Without necking appearance, this deformation process showed a super-plastic deformation character. To our best knowledge, the 200% tensile strain and 2-fold reduction rate in diameter are unprecedented for a SiC NW at low temperature. A schematic model of tensile deformation is illustrated in Figure 5h.

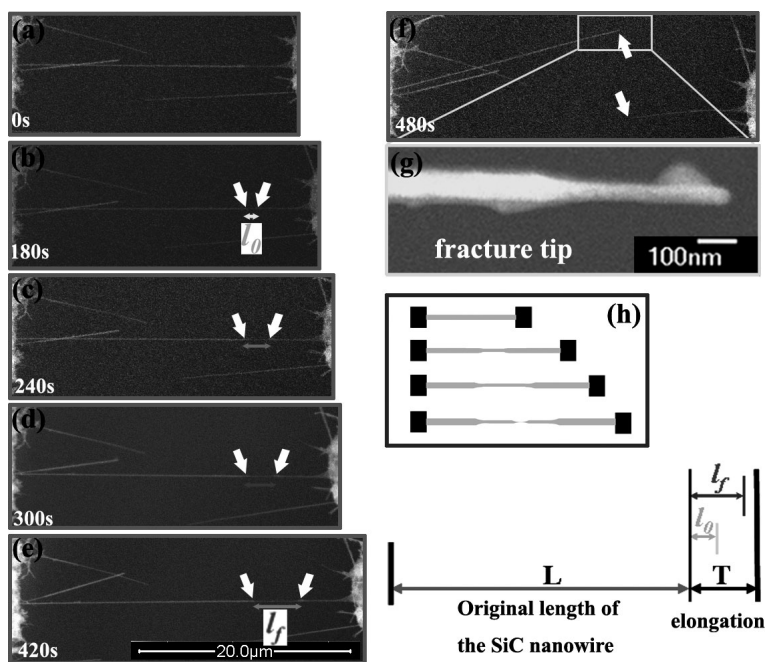


**Figure 5.** a)–f) In situ sequential SEM images showing extensile experiments on an elongated SiC NW. g) A high magnification back scattering electron (BSD) image showing a broken tip. h) Schematic model of the tensile deformation process.

### 2.3. Discussion

We propose that the local super-plastic deformation feature observed is due to inhomogeneous structural feature of the SiC NW. Figure 6a shows a typical TEM image of the 3C-structured SiC NW. Figure 6b shows the HREM images of the two structural modules of the SiC NWs. One is the defect-free segment with perfect cubic (3C) structure, while the other is high defective with a high density of stacking faults. When the SiC NW is pulled in tension, the fundamental deformation mechanism is a shearing action based on the resolved shear stress on active slip systems. The primary slip system is  $\{111\}/\langle 110 \rangle$  for face-centered cubic (FCC) SiC NW with the most favourable Schmidt factor. For the ODD/HD parts of SiC NW, as shown in Figure 6c, the slip systems lie on the (111) plane in which the Schmidt factors are zero. In contrast, there are multiple slip systems such as  $(111)[-110]$  and  $(11-1)[011]$  in 3C structured segments in which the Schmidt factor on one (11-1) plane is 0.272 with respect to the loading axis along [111]. This means that the initial atomic slip was favorable to occur on the type of (11-1) plane of the 3C-structured region when the load was applied along [111] or  $[-1-1-1]$  axial orientation. The subsequent extended tensile process along [111] orientation would result in dislocation nucleation and propagation continuously on the three sets of (11-1), (1-11) and (1-1-1) planes with favorable

Schmidt factors. The dislocation activities were suggested to happen within the region highlighted by the two yellow-blockers as indicated in Figure 6c. It is therefore inferred that a continuous plastic/super-plastic flow resulted in the cubic structural SiC NW segments to continuously transform to be amorphous until fracture failure. The super-plastic flow was confined in the 3C-structured region as illustrated in Figure 6d within the two yellow-blockers as indicated in Figure 6c and d. The ODD/HD segments at the two-ends outside the 3C-structured segment only conducted elastic deformation. As revealed from the direct atomic observation in the previous study,<sup>[27]</sup> the entire plastic deformation process should be three stages: dislocation initiation, dislocation propagation and amorphization. In this study, we revealed one more process of super-plastic flow that follows the amorphization process. Regarding the dislocation initiation and propagation as one integrated process of dislocation activity and includes the super-plastic flow process, we can generalize the plastic deformation and fracture process of SiC NWs to be a quadra-step process, i.e., dislocation activity  $\rightarrow$  amorphization  $\rightarrow$  super-plastic amorphous flow  $\rightarrow$  plastic fracture. These results are entirely consistent with our previous bending deformation by in situ TEM<sup>[27]</sup> and support the theoretical predictions<sup>[22]</sup> of the crystalline to amorphous phase transition procedure of SiC.

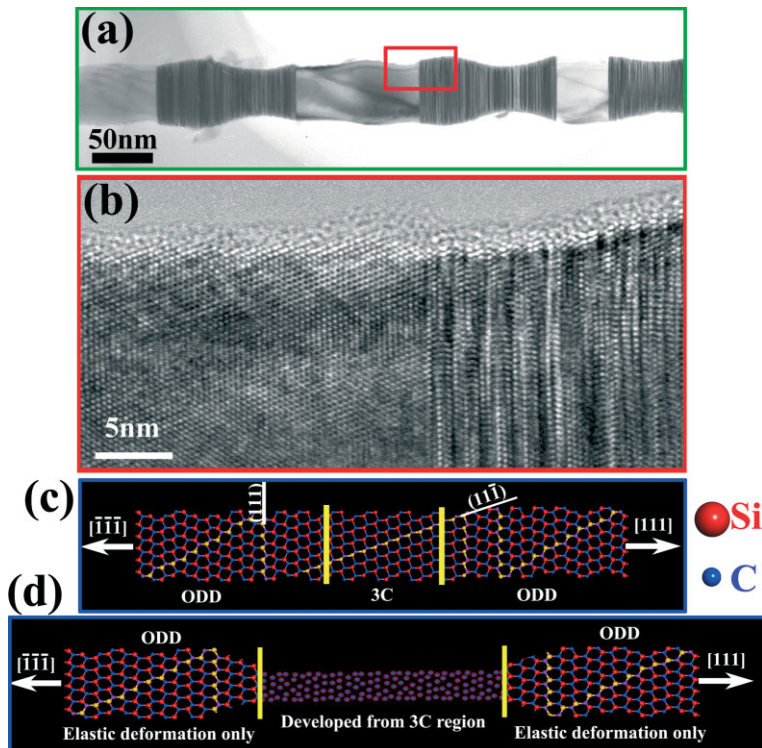


**Figure 6.** a) A typical TEM image of a SiC NW and b) is the HREM image of the 3C and ODD structured segments. c) Is the two-dimensional atomic projection model of a SiC NW with two ODD/HD segments and one 3C segment in the middle. d) Illustration of the atomic model of plastic deformation process in 3C structured segment. The ODD/HD structural parts only conducted elastic deformation. See text for details.

### 3. Summary

These results indicate very distinctive mechanical response of the SiC NWs with 3C and HD structure, respectively. The results of this study provide direct evidence about nanoscale super-plasticity and fracture processes occurring in individual SiC nanowire at low temperature. The high strain plasticity and super-plasticity expected extraordinary toughness in which great amount of energy could be absorbed through the crystalline to amorphous transition and super-plastic flow process. The results anticipated aggressive improvements in fracture toughness of SiC in nano-scale in which 3C-SiC should be a better reinforcing material in ceramics and composites for advanced technological applications. Our results may also provide useful information for further studying of nano-scale brittle-ductile transformation, fracture and strain induced charge-transportation changes of other semiconductor nanowires with large-strain plastic deformation.

### 4. Experimental

The synthesis process of SiC NWs is similar to our previous studies [30,31] which include the xerogel preparation and a subsequent carbothermal reduction. First, 6 g of phenolic resin and 0.5 g of lanthanum nitrate were dissolved in 18 mL of ethanol (AR) and then mixed with 25 mL of tetra-

ethoxysilane (TEOS, AR). Followed, 0.5 mL of hydrochloric acid was added into the mixture, and the mixture was then stirred for up to 30 h to enhance the hydrolysis of TEOS. Finally, 5 mL of hexamethylenetetramine (HMTA, 35.8%) aqueous solution was added into the above mixture for a rapid gelation. The xerogel was obtained by drying the gel product at 110 °C for 12 h. The carbothermal reduction was conducted in a horizontal alumina tubular furnace. The xerogel was heated in Ar flow ( $60 \text{ cm}^3 \text{ min}^{-1}$ ) to 1020 °C at a rate of  $10 \text{ }^\circ\text{C min}^{-1}$ , then to 1320 °C at a rate of  $2 \text{ }^\circ\text{C min}^{-1}$  and maintained at this temperature for 6 h. The raw product was heated in air at 700 °C for 4 h to remove the residual carbon, and subsequently treated by nitric acid ( $\text{HNO}_3$ ) and then hydrofluoric acid (HF) to eliminate the residual silica and other impurities. Some other details regarding the synthesized SiC NWs can be found elsewhere [30,31]. The crystalline structure of the as-synthesized product was evaluated by the X-ray diffraction (XRD) analysis with Cu K $\alpha$  radiation. The product was examined by field emission gun SEM (JEOL JSM-6500F). A small piece of the as-synthesized product was dispersed ultrasonically for 15 min in ethyl alcohol and placed on a Cu supporting carbon microgrid for immediate TEM examination. Conventional TEM analysis and high resolution electron microscopy (HREM) were conducted using a JEOL-2010F operating at 200 kV. Morphology observation and selected-area electron diffraction patterns of the samples were performed. The chemical composition of the samples was detected using energy dispersive X-ray (EDX) spectroscopy and electron energy loss spectroscopy (EELS).

Received: February 7, 2007

Revised: March 30, 2007

Published online: October 16, 2007

- [1] O. D. Sherby, J. Wadsworth, *Deformation, Processing and Structure* (Eds: G.Krauss), ASM Int., Metals Park, OH **1984**.
- [2] C. J. Shih, M. A. Meyers, V. F. Nesterenko, S. J. Chen, *Acta Mater.* **2000**, *48*, 2399.
- [3] D. J. Green, *An Introduction to the Mechanical Properties of Ceramics*, Cambridge University Press, Cambridge **1998**.
- [4] P. Pirouz, M. Zhang, J. L. Demenet, H. M. Hobgood, *J. Phys. Condens. Matter* **2002**, *14*, 12929.
- [5] P. B. Hirsch, S. G. Roberts, *Acta Mater.* **1996**, *44*, 2361.
- [6] B. Wu, A. Heidelberg, J. J. Boland, *Nat. Mater.* **2005**, *4*, 525.
- [7] P. Poncharal, Z. L. Wang, D. Ugarte, W. A. D. Heer, *Science* **1999**, *283*, 1513.
- [8] E. W. Wong, P. E. Sheehan, C. M. Liber, *Science* **1997**, *277*, 1971.
- [9] K. Lu, M. L. Sui, *Scr. Metall. Mater.* **1993**, *28*, 1465.
- [10] H. K. Seong, H. J. Choi, S. K. Lee, J. I. Lee, D. J. Choi, *Appl. Phys. Lett.* **2004**, *85*, 1256.
- [11] Z. W. Pan, H. L. Lai, F. C. K. Au, X. F. Duan, W. Y. Zhou, W. S. Shi, N. Wang, C. S. Lee, N. B. Wong, S. T. Lee, S. S. Xie, *Adv. Mater.* **2000**, *12*, 1186.
- [12] X. H. Sun, C. P. Li, W. K. Wong, N. B. Wong, C. S. Lee, S. T. Lee, B. K. Teo, *J. Am. Chem. Soc.* **2002**, *124*, 14464.
- [13] A. M. Leach, M. McDowell, K. Gall, *Adv. Funct. Mater.* **2007**, *17*, 43.
- [14] P. X. Gao, W. Mai, Z. L. Wang, *Nano Lett.* **2006**, *6*, 2536.
- [15] R. He, P. Yang, *Nat. Nanotechnol.* **2006**, *1*, 42.
- [16] J. Li, J. K. V. Vliet, T. Zhu, S. Yip, S. Suresh, *Nature* **2002**, *418*, 307.
- [17] K. S. Cheung, S. Yip, *Phys. Rev. Lett.* **1990**, *65*, 2804.
- [18] Z. Wang, X. Zu, F. Gao, W. J. Weber, *Appl. Phys. Lett.* **2006**, *89*, 243123.
- [19] H. Kikuchi, R. K. Kalia, A. Nakano, P. Vashishta, P. S. Branicio, F. Shimojo, *J. Appl. Phys.* **2005**, *98*, 103524.
- [20] M. Tang, S. Yip, *J. Appl. Phys.* **1994**, *76*, 2719.
- [21] T. Y. Kim, S. S. Han, H. M. Lee, *Mater. Trans.* **2004**, *45*, 1442.
- [22] W. Li, R. K. Kalia, P. Vashishta, *Phys. Rev. Lett.* **1996**, *77*, 2241.
- [23] X. D. Li, X. N. Wang, Q. H. Xiong, P. C. Eklund, *Nano Lett.* **2005**, *5*, 1982.
- [24] X. D. Li, H. S. Gao, C. J. Murphy, K. K. Caswell, *Nano Lett.* **2003**, *3*, 1495.
- [25] J. Y. Huang, S. Chen, Z. Q. Wang, K. Kempa, Y. M. Wang, S. H. Jo, G. Chen, M. S. Dresselhaus, Z. F. Ren, *Nature* **2006**, *439*, 281.
- [26] X. D. Han, Y. F. Zhang, Z. Zhang, Y. J. Hao, X. Y. Guo, *J. Appl. Phys.* **2005**, *98*, 124307.
- [27] X. D. Han, Y. F. Zhang, K. Zheng, Z. Zhang, Y. J. Hao, X. Y. Guo, J. Yuan, Z. L. Wang, *Nano Lett.* **2007**, *7*, 452.
- [28] J. M. Cowley, A. F. Moodie, *Acta Crystallogr.* **1957**, *10*, 609.
- [29] T. L. Daulton, T. J. Bernatowicz, R. S. Lewis, S. Messenger, F. J. Stadermann, S. Amari, *Geochim. Cosmochim. Acta* **2003**, *67*, 4743.
- [30] G. Q. Jin, P. Liang, X. Y. Guo, *J. Mater. Sci. Lett.* **2003**, *22*, 767.
- [31] Y. J. Hao, G. Q. Jin, X. D. Han, X. Y. Guo, *Mater. Lett.* **2006**, *60*, 1334.